Experimental Thermal and Fluid Science 112 (2020) 109949

Contents lists available at ScienceDirect

Experimental Thermal and Fluid Science

journal homepage: www.elsevier.com/locate/etfs

Void fraction and speed of sound measurement in cavitating flows by the three pressure transducers (3PT) technique

Claudia Esposito[a,b,*], Onur Yenigun[c], Jean-Baptiste Gouriet[a], Johan Steelant[b,d], Maria Rosaria Vetrano[b]

[a] von Karman Institute for Fluid Dynamics, Chaussée De Waterloo 72, B-1640 Rhode-St-Genèse, Belgium
[b] KU Leuven, Celestijnenlaan 300A postbus 2421, B-3001 Heverlee, Belgium
[c] Department of Mechanical Engineering, Izmir Institute of Technology, 35430 Izmir, Turkey
[d] Aerothermodynamics and Propulsion Analysis Section, ESTEC-ESA, Keplerlaan 1, 2200AG Noordwijk, the Netherlands

ARTICLE INFO

Keywords:
Speed of sound
Cavitating flow
Pressure transducers
Void fraction

ABSTRACT

Speed of sound and void fraction are two key parameters in the characterisation of two-phase flows. However, accurate measurements require either intrusive or complex techniques. This paper reports on the Three Pressure Transducers (3PT) technique, which derives the speed of sound by measuring pressure fluctuations and which, thanks to its robustness and simplicity, could be applicable in harsh conditions. Therefore, the aim of this paper is to study in detail the feasibility of this technique against its limits and constraints in a cavitating flow. First, a numerical assessment of the technique is proposed to determine both the optimal transducers configuration and the sampling frequency. Then, the implemented algorithm was applied to a two-phase air–water mixture with well-known properties. Finally, the 3PT algorithm was used to study the behaviour of a cavitating flow induced by an orifice. This last application highlighted the possibility to use this technique to characterize the bubble flow generated by an orifice without the use of any optical access and by using a very compact experimental arrangement. The results obtained are also qualitatively compared to the images of the flow simultaneously acquired by a high-speed camera.

1. Introduction

Hydrodynamic cavitation through orifices and nozzles has been largely investigated in literature. Despite the popularity and the quite simple geometry which is involved, this problem is still widely studied both numerically and experimentally. The complexity of this subject involves different aspects. A crucial one is the determination of the speed of sound (c) and the void fraction (α) during the various cavitating regimes. These two parameters are strongly related to each other: the sudden increase in the vapour content due to the development of cavitation leads to deep variations in the speed of sound. As an example, Jakobsen [1] found that the speed of sound for cold water, which is around 1500 m/s in fully liquid conditions, could decrease to 3.3 m/s in a two-phase mixture. Hence, if on one hand measuring the void fraction produced by cavitation is necessary to properly design valves and restrictions in hydraulic systems, on the other hand, it provides a way to estimate the speed of sound and to better understand the physics behind cavitation mechanisms. Specifically, as reported in Danlos et al. [2], measuring the speed of sound is of great interest when investigating the flow instabilities in the cloud cavitation regime, that happens when the cavity, i.e. the vapour cluster, becomes unstable and the vapour clouds are shed downstream causing noise and vibrations. The flow instabilities linked to the cloud cavitation regime have been studied by researchers as Ganesh et al. [3] and Callenaere et al. [4] and the experimental work by Jahangir et al. [5] has shown the cases in which these instabilities are driven by a shock wave mechanism due to the abrupt drop in the speed of sound. Many efforts in measuring the minimum speed of sound (c_{min}) have also been done to improve numerical simulations. Indeed, many homogeneous mixture models use a barotropic law (Goncalves and Patella [6], Decaix and Goncalves [7],Örley et al. [8]) to close the system of Euler equations and such law includes the minimum speed of sound. In Coutier-Delgosha et al. [9] a proper estimation of this value is considered essential to reproduce the cavity shapes obtained during experiments. However, a correct estimation of this (c_{min}) is still matter of discussion and combined measurements of both parameters are often used in literature.

As far as the void fraction is concerned, having measurements both accurate and easy to implement is still a big challenge. Light-

* Corresponding author.
E-mail address: claudia.esposito@vki.ac.be (C. Esposito).

https://doi.org/10.1016/j.expthermflusci.2019.109949
Received 11 June 2019; Received in revised form 2 October 2019; Accepted 6 October 2019
Available online 22 October 2019
0894-1777/

Nomenclature

Abbreviations

3*PT*	Three Pressure Transducers
FOV	Field of view
RMSE	Root mean square error
$T1$, $T2$, $T3$, $T4$, $T5$	test cases
$V1$, $V2$	Valves

List of Subscripts

conf	confined to the pipe
cri	critical
dw	downstream
exp	experimental
free	free environment
i	imaginary
in	input
L	left
l	liquid
out	output
R	right
r	real
sat	saturation
th	theoretical
up	upstream
v	vapour

List of Symbols

C	complex amplitude
c	speed of sound
D	pipe diameter
d	orifice diameter
E	elasticity
e	pipe thickness
f	frequency
F_f	liquid critical pressure ratio
F_L	liquid pressure recovery factor
f_s	sampling frequency
G	power spectral density
H	transfer function
k	wavenumber
K_v	flow coefficient
L	generic length
M	Mach number
N	noise level
N_s	number of samples
n	polytropic index
P	pressure
$\hat{P}$	non dimensional pressure
Q	flow rate
$\hat{Q}$	non dimensional flow rate
Q_{max}	choked flow rate
S	generic signal
s	orifice thickness
T	temperature
U	velocity
X	random signal
x	flow quality
α	void fraction
β	orifice characteristic ratio
γ	coherence function
Δ	discrepancy
ν	Poisson ratio
ρ	density
σ	standard deviation
ω	angular frequency

attenuation technique has been used by Leppinen and Dalziel [10] for low cavitating flows. Attenuation of light passing through the bubbly flow is captured by a CCD camera and the void fraction is correlated to the transmittance of light in presence of vapour. However, Leppinen and Dalziel [10] showed that this technique is only valid when the bubble size distribution in the bubbly flow is controlled and kept constant during the experiment. Moreover, as the void fraction increases, optical methods are not reliable anymore. An alternative is to use electrical impedance probes. Since gas and liquid have different electrical properties, void fraction can be deduced either by the local or by the average mixture impedance. At this purpose, flush-mounted electrodes (e.g., Ceccio and Brennen [11], George et al. [12]) or intrusive probes (e.g., Wu and Ishii [13], Elbing et al. [14], Lucas and Mishra [15]) are proposed. Fiber optic probes have also been successfully applied by Coutier-Delgosha et al. [16] and Stutz and Reboud [17] to measure the average void fraction and to study the two-phase flow morphology. Unfortunately, these probes are fragile and intrusive, thus, their use is limited and not suitable for cavitating flows. Another possibility is represented by X-rays radiation-based techniques. These have been widely used in the last years and their application in two-phase has been reviewed by Heindel [18]. During the last years, these techniques evolved into the X-rays computed tomography (Bauer and Chaves [19], Jahangir et al. [5]), which has the advantage of measuring both the void fraction spatial average and the void fraction along a cross section. On the other hand, its application is limited by the complexity of its hardware. As far as speed of sound is concerned, Hassis [20] and Henry et al. [21] directly measured it with pressure sensors. This work aims to evaluate the suitability of the Three Pressure Transducers (3PT) technique for measuring the speed of sound in a cavitating flow induced by an orifice. This technique provides averaged values of void fraction both in time and in space. However, its ease of application, since it requires only three unsteady pressure sensors, makes it attractive. Besides, it allows measurements even for those cases where optical access is not possible. Hence, it can be of large interest in the industrial domain where the monitoring and the rapid detection of cavitation are of primary importance. Indeed, at the author's knowledge, there are no other means to observe or predict the behaviour of cavitation in a pipe apart from optical visualizations or measurements of pipes vibrations, which can be affected by many environmental causes.

The 3PT has been patented in 2004 by Gysling and Myers [22] and allows to retrieve the sound velocity in a confined medium by measuring the fluctuations of the pressure waves which propagate in that medium. This technique was first developed in the 1970s by Margolis and Brown [23] to study the propagation of long-wavelength disturbances through turbulent flows in pipes. The method relies on the assumption that pressure waves propagate through a pipe without changing their amplitude. Therefore, this assumption limits the technique up to a cut-off frequency beyond which pressure waves do not propagate anymore as plane waves. Moreover, as it will be explained in the following sections, it influences the relative position of the pressure sensors too.

This technique was successfully applied by Testud et al. [24] and Shamsborhan [25] to calculate the speed of sound in both single phase and cavitating flow induced by either single or multiple holes orifices. With a different purpose, Kashima et al. [26] and Blommaert [27]

adopted the 3PT to measure both high-speed discharges and speed of sound fluctuations in pressurized lines. Recently, Simon et al. [28] have proposed a new data analysis algorithm for the 3PT technique based on the least mean squares method. This algorithm gave good results in the full range of velocities from 100 to 1400 m/s.

This paper is composed of 7 sections including this Introduction. Section 2 describes the technique and details its mathematical and physical background. The implementation of the method and its uncertainties are analysed in Section 3. Section 4 describes the experimental set-up and the selected orifice geometries. Section 5 is devoted to explaining the application of the technique with a two-phase two-species mixture, obtained by injecting a known amount of air bubbles into a fully liquid flow. The speed of sound measurements during cavitation experiments are pictured in Section 6 where an attempt to extract the void fraction is shown too. Finally, the main conclusions are drawn in Section 7.

2. The 3 Pressure Transducers technique

The acoustic pressure field induced by singularities in a hydraulic system $p(x, t)$ can be written as the superposition of a forward and a backward travelling wave if the wavelength λ of the acoustic waves is long compared to the diameter of the pipe (Gysling and Myers [22], Margolis and Brown [23], Shamsborhan [25]):

$$p(x, t) = C_1 e^{j(\omega t + kx)} + C_2 e^{j(\omega t - kx)} \tag{1}$$

where $k = \omega/c$ is the wavenumber, c is the speed of sound in the medium and the constants C_1 and C_2 are frequency-based complex amplitudes.

The frequency domain representation of the time-varying pressure signal $p(x, f)$ can be expressed by:

$$p(x, f) = C_1(f) e^{jkx} + C_2(f) e^{-jkx} \tag{2}$$

Let us now consider a pipe and three values of pressure obtained in three different locations separated by a distance L (see Fig. 1). The following system of equations can be written:

$$\begin{aligned} p_1 &= p(-L, f) = C_1(f) e^{-jk_{conf}L} + C_2(f) e^{jk_{conf}L} \\ p_2 &= p(0, f) = C_1(f) + C_2(f) \\ p_3 &= p(L, f) = C_1(f) e^{jk_{conf}L} + C_2(f) e^{-jk_{conf}L} \end{aligned} \tag{3}$$

where now $k_{conf} = \omega/c_{conf}$ and c_{conf} is the speed of sound confined to the pipe volume. By the definition of the variable H, which reduces to a cosine signal since its imaginary part is null, it is possible to relate the sound confined to the pipe volume, c_{conf}, to the pressures in the pipe.

$$H = \frac{p_1 + p_3}{2 \cdot p_2} \tag{4}$$

$$H = Re(H) = \cos\left(k_{conf} L\right) = \cos\left(\frac{\omega \cdot L}{c_{conf}}\right) \tag{5}$$

To derive the void fraction from the speed of sound, several correlation laws exist in literature. One of the most recent relationships is the one recommended by Brennen [29] which includes both mass and heat exchanges and it reads

$$\frac{1}{c^2} = [\alpha \cdot \rho_v + (1 - \alpha) \cdot \rho_l] \cdot \left[\frac{\alpha}{n \cdot P} + \frac{1 - \alpha}{\rho_l \cdot c_l^2}\right] \tag{6}$$

where the subscripts v and l stand for the vapour and liquid phase respectively. The term n is the polytropic coefficient which allows taking into account both the isothermal ($n = 1$) and the adiabatic case ($n = 1.4$). Fig. 2 shows an example of this relation in both the adiabatic and the isothermal case at $P = 13000$ Pa and $T = 302$ K. A minimum of 7 and 8 m/s is reached at $\alpha = 0.5$ for isothermal and adiabatic, respectively.

The speed of sound (c) in Eq. (6) is the one in free environment (c_{free}), whereas the computed one is confined to a pipe (c_{conf}). By considering the compressibility of the fluid and the pipe properties, Lighthill [30] explicits the relation between c_{conf} and c_{free} as:

$$c_{free} = c_{conf} \cdot \left[1 - \frac{D}{eE}(1 - \nu^2) \cdot c_{conf}^2 \cdot (\alpha \cdot \rho_v + (1 - \alpha) \cdot \rho_l)\right]^{-0.5} \tag{7}$$

where D is the pipe diameter, E is the elasticity of the pipe, e is its thickness, ν is the pipe Poissons ratio, and finally, α is the void fraction and the mixture is supposed homogeneous.

Experiments performed by Shamsborhan [25] and Costigan and Whalley [31] for a two-phase two-species mixture (e.g. water–air) have given results in good agreement with this model. Shamsborhan's measurements [25] in a two-phase one-species mixture appeared to fall between these two curves. Consequently, within this work, a first estimation of the void fraction will be provided based on Brennen formulation and the uncertainty will be given by the discrepancy between the two cases, isothermal and adiabatic.

2.1. Mach number effect

Gysling and Myers [22] and Shamsborhan [25] pointed out that for flows at high Mach number ($M > 0.9$) the wave numbers of the upstream travelling wave and the downstream travelling one should differ. Due to the mean flow velocity, a convective Doppler bias exists: pressure waves travelling downstream (k_{dw}) are faster than those going upstream (k_{up}). This leads to the definitions given in Eq. (8) and Eq. (9).

$$k_{dw} = \frac{\omega}{c} \cdot \frac{1}{1 + M_x} \tag{8}$$

$$k_{up} = \frac{\omega}{c} \cdot \frac{1}{1 - M_x} \tag{9}$$

When the mean axial velocity of the flow is small compared to the speed of sound, the two pressure waves are supposed to travel with the same velocity ($k = k_{up} = k_{dw}$). This hypothesis becomes uncertain in developed cavitation conditions where the speeds of sound are extremely low.

In addition, two-phase damping studied by Carlucci and Brown [32] and Charreton et al. [33] becomes predominant while increasing the void fraction and the formulation of the variable H suggested by Hassis [20] is:

$$\begin{aligned} H \;&= \cos(k_{dw}^r \cdot L) \cdot e^{k_{dw}^i \cdot L} + \cos(k_{up}^r \cdot L) \cdot e^{-k_{up}^i \cdot L} + \\ &+ i\sin(k_{dw}^r \cdot L) \cdot e^{k_{dw}^i \cdot L} - i\sin(k_{up}^r \cdot L) \cdot e^{-k_{up}^i \cdot L} \end{aligned} \tag{10}$$

The superscripts r and i in Eq. (10) stand for the real and imaginary part respectively.

3. Numerical implementation and parametric study

To determine the robustness of the technique, a first numerical assessment was performed by using synthetic pressure signals. The parameters chosen for this assessment are defined in Eq. (5) and they are as follows: the distance between two consecutive pressure transducers (L), the sampling frequency (f_s), and the noise level (N). For this

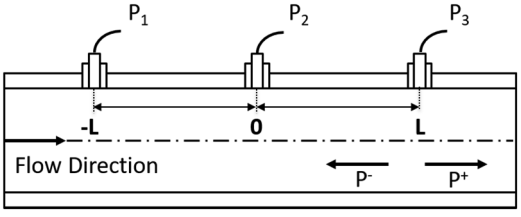

Fig. 1. Schematic for the three pressure transducers technique.

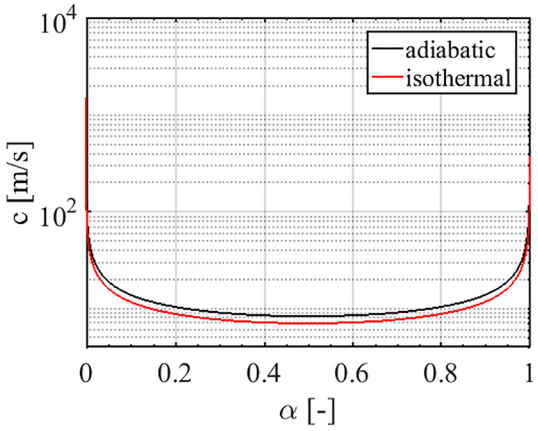

Fig. 2. Relationship between the speed of sound and the void fraction according to the Brennen formulation (Eq. (6)), for both the adiabatic and the isothermal case in water at $P = 13000$ Pa. and $T = 302$ K.

assessment, the following procedure was used. Synthetic pressure waves corresponding to speeds of sound c_{in} ranging from 10 m/s to 1500 m/s were generated by means of Eq. (2). This range covers most of the possible speeds encountered in a liquid–vapour water mixture. Subsequently, we used a data inversion algorithm based on the inverse Fourier transform to derive the pressure signals in the time domain. Such signals are used as input for another algorithm that implements the 3PT technique and computes the speed of sound (c_{out}). Finally, the reliability of the algorithm was established by comparing the c_{out} to the c_{in}.

Firstly, the effect of the sampling frequency value on the quality and on the reliability of the c_{out} is discussed. The considered sampling frequencies range from 26 kHz to 110 kHz. The lower limit is equal to the cut-off frequency for plane waves in a pipe with a diameter D of 40 mm, like the one used for the experiments illustrated in Section 4. The higher limit was set based on the acquisition system capabilities. Fig. 3 compares the results of these simulations for six different input speeds of sound which have not been polluted by noise. On the vertical axis the percentage discrepancy between c_{out} and c_{in}, $\Delta c = \left|\frac{c_{out} - c_{in}}{c_{in}}\right|$, is shown. At low c_{in} the algorithm provides good results already at 26 kHz with Δc below 5%. As c_{in} increases, the algorithm needs higher sampling frequencies to provide accurate results.

A critical point of the technique is that it requires an equal distance between the three pressure transducers. Two analyses were then performed. One concerned the absolute value of the distance L between the sensors and another the small deviations from this value due to manufacturing. Calculations were carried out with nine different values of L ranging from $L = D$ to $L = 3D$. Table 1 reports the values of Δc computed for three exemplary distances (L) in the considered range at four values of speed of sound. At 50 m/s the differences between c_{out} and c_{in} in the three cases are comparable. Nevertheless, as the velocity increases, the error in the calculations reduces for longer distances between the sensors.

Possible manufacturing errors could compromise the applicability of the technique due to the inaccurate positioning of the pressure sensors. This problem was addressed by progressively increasing the distance between two consecutive signals of small quantities going from 2% to 10% of its initial value. It has been observed that errors in the distance up to 2% lead to a maximum discrepancy between c_{out} and c_{in} of around 10%. For errors bigger than 8% of L, the trigonometric relation to compute H (Eq. (5)) yields no result. Therefore, it is crucial to accurately respect the sensor symmetry.

The last contribution is the one due to the noise polluting the pressure waves. To analyse this contribution, the synthetic signals were corrupted by Gaussian noise to simulate a realistic case.

The added noise has been defined according to Eq. (11), where S is the original signal, N is the noise level, ranging from 5% to 50%, and X a random signal whose dimension is the same as S.

$$\Delta S = S \cdot N \cdot \frac{X}{\sigma_X} \tag{11}$$

As a result, the minima of the H functions, Eq. (4), are not anymore well defined, see Fig. 4. Therefore, the algorithm includes a zero-phase low pass filter and a new function H_{filt} is obtained to detect the minimum. Fig. 4 shows a comparison between S and the corresponding $S + \Delta S$ with 50% of noise. The presence of noise seems to have a stronger impact at low speeds. For example, at 50 m/s (Fig. 5.a) the algorithm gives more accurate results but the uncertainty increases with the level of noise. On the other hand, at 1500 m/s (Fig. 5.b) the effect of noise is almost negligible compared to the error already introduced because of the sampling frequency and the distance.

3.1. Choice of the optimal parameters configuration

The combined effect of the investigated parameters () is discussed in this section. Fig. 6 shows the results obtained when the target is to measure a speed of sound of 50 m/s. In this case, the algorithm provides quite accurate results regardless of the three analysed parameters. The overall error reaches peaks between 7% and 11% at levels of noise higher than 40%.

By increasing the speed of sound (Fig. 7), the effect of both the sampling frequency and the transducers distance start to be highlighted. The overall error on the speed of sound reduces for increasing values of f_s and L. At 1500 m/s (Fig. 8), the error induced by the noise is negligible with respect to that due to the sampling frequency and the transducers distance. As a general behaviour, the efficiency of the algorithm deteriorates for high speed flows, especially at low sampling frequencies (errors up to 40%). Even if the performances of the algorithm improve increasing the distance L, this does not fully compensate for the deterioration due to the sampling frequency.

According to these results, a sampling frequency of 100 kHz was selected to acquire the pressure data during the entire experimental campaign. Despite the large amount of data generated by this frequency, it led to the following Δc discrepancies in the results: 11% for speeds of sound around 1500 m/s (single phase fully liquid), and 4% for low velocities up to 500 m/s.

As for the transducers distance, the one of $1.5D$, namely 0.06 m, was chosen as a result of a trade-off. Previous results showed that larger distances provide better results. However, this intermediate spacing of 0.06 m was preferred because larger distances could compromise the

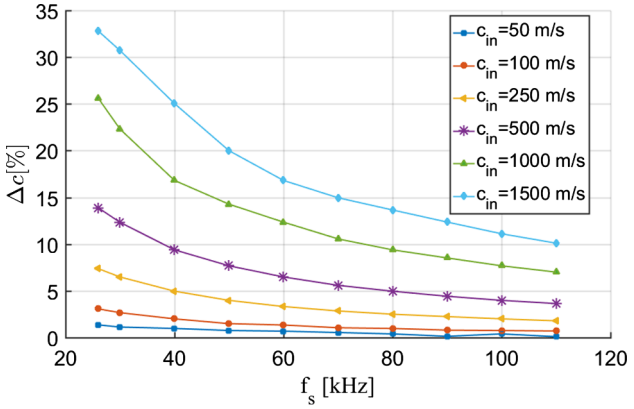

Fig. 3. Percentage deviation between c_{out} and c_{in} as a function of the sampling frequency for different speed of sound values with $L = 1.5D$.

Table 1
Δc computed at three exemplary signal locations and four c values.

	L = D	L = 1.5D	L = 3D
c = 50 m/s	0.39%	0.39%	0.34%
c = 500 m/s	5.86%	3.98%	2.00%
c = 1000 m/s	11.11%	7.68%	3.98%
c = 1500 m/s	15.48%	11.10%	5.86%

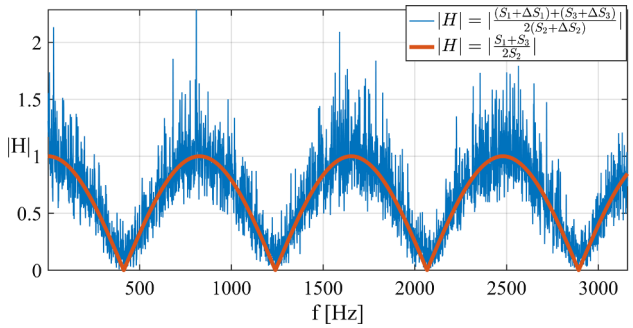

Fig. 4. H function obtained from the clean signal (S) and from the noise signal (with N = 50%) for c_{in} = 100 m/s.

hypothesis of homogeneous flow during real measurements in cavitating conditions. These parameters led to the following discrepancies in the results: 14% for speeds of sound around 1500 m/s (single phase fully liquid), and 4% for low velocities up to 500 m/s.

Finally, the effect of the noise level is to be taken into account only for low speeds of sound and it reduces by the filtering included in the algorithm. When the noise level was increased up to 50%, the error on the calculated speed of sound varied maximum of ± 7%.

4. Experimental facility

The experimental facility used in this work is shown in Fig. 9. It is a water closed loop where water is stored in a 750 litres tank connected to a vertical cylindrical test section in which different types of singularities can be installed. The test section is in acrylic glass (E = 3300·10^6 N/m^2,ν = 0.37) with an inner diameter D = 40 mm and wall thickness e = 20 mm. The inner and outer surfaces of the test section are polished, which allows a proper visualization of the cavitation flow. Between the reservoir and the test section, a 100 litres calming reservoir is installed in order to separate the remaining gas pockets and to have a fully liquid flow in the test section. A fluid pump is installed into the loop to put the fluid into circulation, while a vacuum pump is used to both degas the water and set specific pressure conditions. The main water reservoir is also equipped with an electrical resistance which is used to warm the water up to 50 °C for a more rapid degassing. The level of oxygen present in the water during the tests is monitored by means of an oxygen probe installed in the calming reservoir. The mass flow rate is measured with an ABB Magmaster electromagnetic flowmeter placed upstream the test section. A Valydine (0.25% full-scale accuracy) has been employed to measure the pressure inlet conditions 5D upstream of the orifice. The outlet conditions are measured at a distance of 7.9D downstream of the orifice. The test-section is instrumented with three unsteady pressure transducers (XTL-M Kulites 0.1% full-scale accuracy) which will be used for the 3PT technique. They are positioned downstream of the orifice at 4.9D, 6.4D and 7.9D, respectively. The spacing of 60 mm between consecutive transducers and an acquisition frequency of 100 kHz have been set according to the parametric study explained in Section 3.

Being the test section made of acrylic glass, the maximum operating pressure of the whole facility is 500 kPa abs. The back-pressure is adjusted either slightly by a valve located downstream of the test section (V2), or by the vacuum pump which is connected to the top of the reservoir; a minimum back-pressure of 10 kPa abs can be achieved. Two orifice geometries have been tested (Fig. 10). The first one is a cylindrical sharp-edged thick orifice with a ratio between the orifice diameter (d) and the pipe diameter (D) $\beta = \frac{d}{D}$ = 0.17 and a non dimensional thickness s/d = 1.2. The second geometry is conical with β = 0.16 and the aperture angle of 126°.

The flow is visualized at two different locations of the test section. A first high-speed camera records images at a frequency of 14 kHz immediately downstream of the orifice (region *FOV* 1). A second high-speed camera is positioned 4D downstream of the orifice to visualize the whole region in which the three-pressure transducers are placed (region *FOV* 2) at a frequency of 1 kHz. The cameras are synchronized with the sensors used for the 3PT technique. The water temperature and the dissolved amount of oxygen are measured in the calming reservoir with a thermocouple type K and a Vernier Optical DO probe.

5. Assessment of the 3PT technique for air–water bubbly flow

The calibration of the 3PT technique was done by using the additional line sketched in Fig. 11. A needle with three equidistantly spaced holes was mounted at the end of this line to supply a known homogeneous flow rate of air while water was gently flowing in the test section. By varying the air flow rate, different levels of flow quality x were set ranging from 0.5% to 4% of the total volumetric flow rate. As already expected from the experimental works of Hewitt and Roberts [34] and Taitel et al. [35], these values corresponded to a bubbly flow,

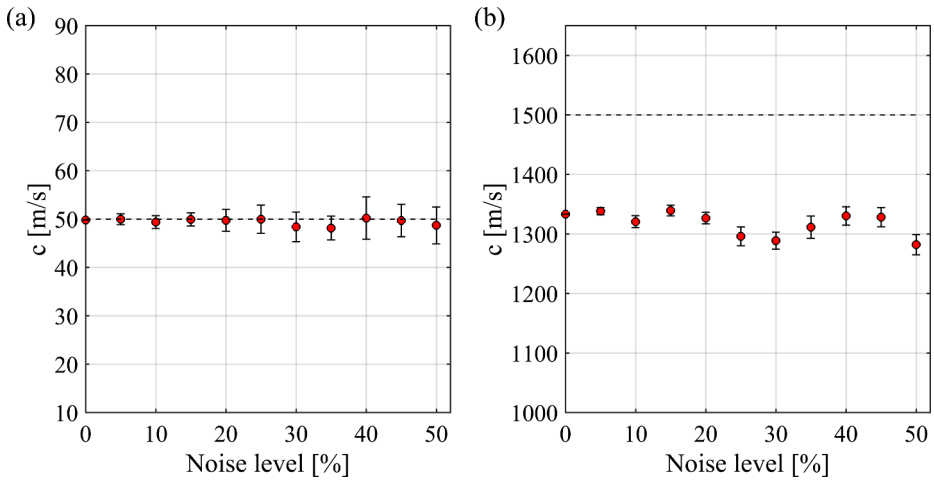

Fig. 5. Examples of calculated speeds of sound at increasing levels of noise for two different cases: (a) c_{in} = 50 m/s and L = 1.5D; (b) c_{in} = 1500 m/s and L = 1.5D.

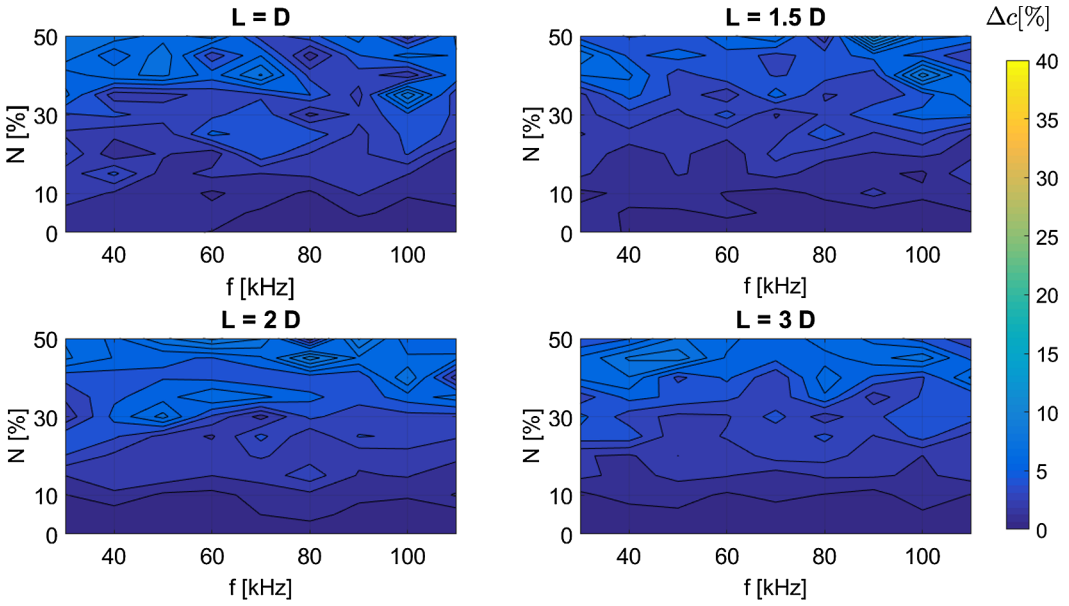

Fig. 6. Validation results at 50 m/s with the error in the calculation of the speed of sound mainly dependent on the noise level: $max\left(\frac{|c_{out}-c_{in}|}{c_{in}}\right) \leqslant 11\%$ for $N \geqslant 40\%$.

Fig. 13(bottom). These low values of x justify the assumption of $\alpha = x$. Specifically, the hypotheses of the homogeneous flow model and mechanical equilibrium are valid at low x and they allow to simplify the correlations for α as also shown by Chisholm [36] or Smith [37]. Ten pressure signals, each corresponding to 1 s of acquisition time, have been recorded. The H functions are then computed and averaged as shown in Fig. 12.

The repeatability was verified by performing each measurement three times. Fig. 13 depicts the comparison between the imposed void fraction (α_{exp}) and the one obtained by the 3PT technique (α_{calc}). These void fraction values correspond to speeds of sound of the water–air mixture ranging between 60 and 160 m/s.

To quantify the uncertainty on the measures from the 3PT, another quantity has also been computed for each condition: the root mean square error (RMSE) between the obtained H function (H_{out}) and the theoretical one (H_{th}), Eq. (12). H_{th} is the theoretical H function obtained by imposing the speed of sound resulting from the H_{filt}. The RMSE increases with both the level of noise and the speed of sound. Noise levels of 50% correspond to a RMSE which ranges from 0.120 to 0.146, depending on the speed of sound. Fig. 14 shows the comparison between H_{out} and the theoretical H function at $c = 1500$ m/s ($RMSE = 0.146$).

$$RMSE = \sqrt{\frac{1}{N_s}\cdot\sum_{i=1}^{N_s}\left(H_{exp}(i) - H_{th}(i)\right)^2} \tag{12}$$

Summarizing, we set two thresholds in terms of RMSE. Up to $RMSE = 0.05$, which corresponds to $N = 20\%$, only the systematic error on the measured c is considered. At higher RMSEs the random error due to the addition of noise is also taken into account. Hence, the error bars in Fig. 13 include both the systematic error and the random error since the obtained H function has an RMSE ranging from 0.10 to 0.17.

The bottom part of Fig. 13 shows three examples of the

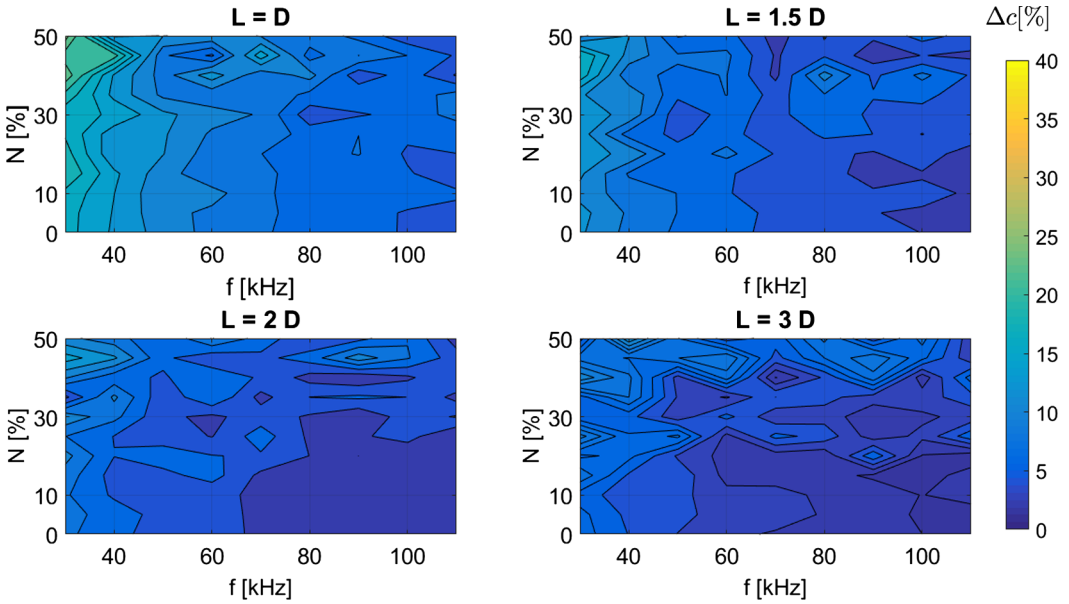

Fig. 7. Validation results at 500 m/s with the error in the calculation of the speed of sound increasing at smaller distances between the sensors and lower sampling frequencies.

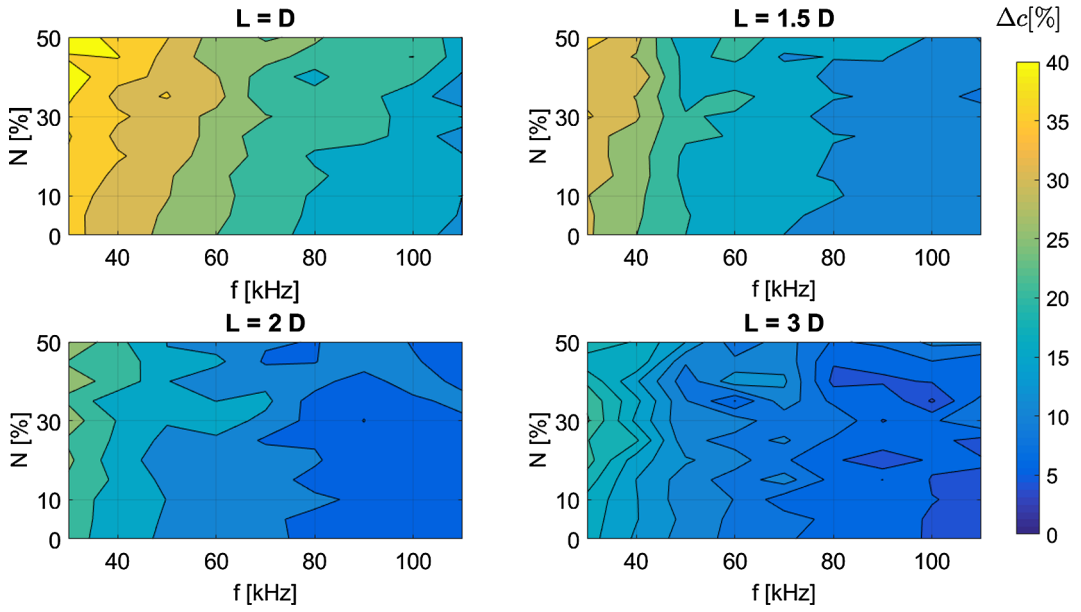

Fig. 8. Validation results at 1500 m/s with the error in the calculation of the speed of sound mainly dependent on the sampling frequency and the sensors position: $max\left(\frac{|c_{out}-c_{in}|}{c_{in}}\right) \approx 40\%$ for $L = D$ and $f_s \leq 30$ kHz.

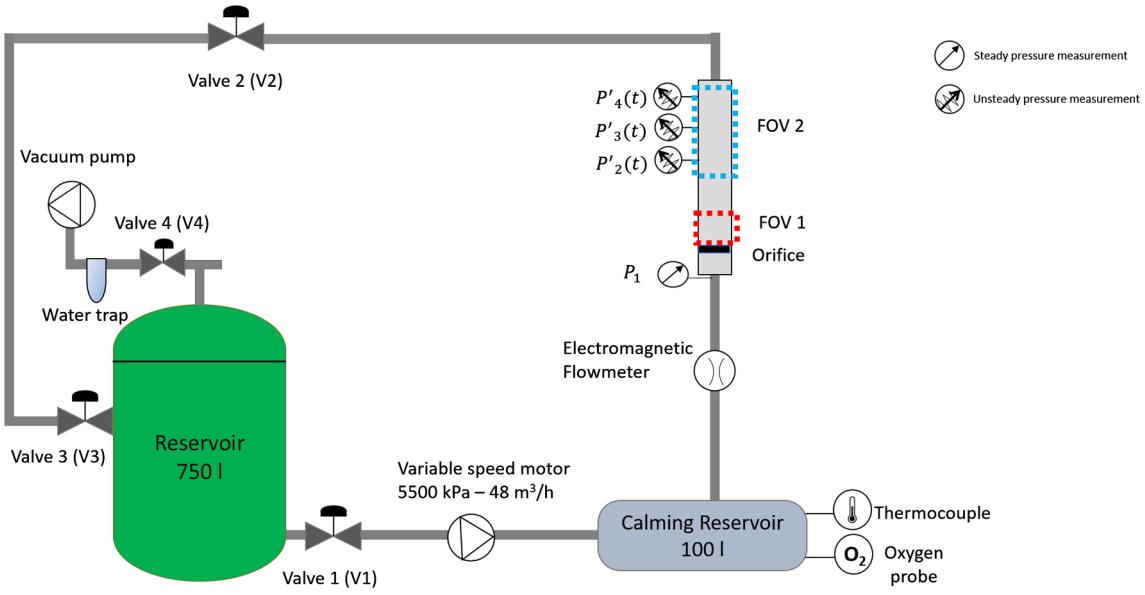

Fig. 9. Schematic of the water closed loop facility with transparent test-section instrumented with the three unsteady pressure sensors downstream of the orifice.

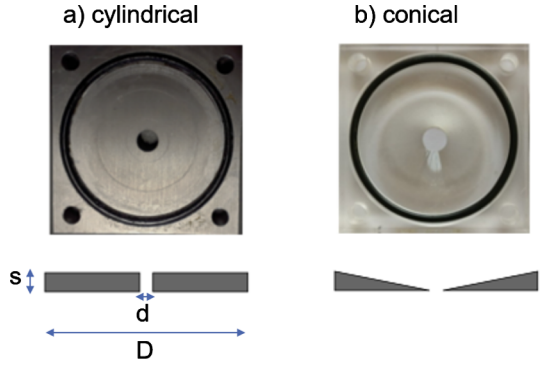

Fig. 10. Orifice geometry: a) cylindrical orifice; b) conical orifice.

visualizations performed in *FOV* 2. These visualizations show a homogeneous two-phase flow distribution. The bubbles size is controlled by the needle, thus the increase in the void fraction is linked to the increase in the number of bubbles.

6. Measurements in cavitating conditions

6.1. Cavitating conditions

When applying the technique to cavitation, the occurrence of different flow regimes has to be considered. Mainly, three regimes can be distinguished: incipient cavitation, cloud cavitation and super-cavitation ([38–40]). The occurrence of one regime rather than another is dictated by mainly three non-dimensional parameters: β , Re and $\hat{P}$. The smaller β is, the lower the Re and pressure drops needed to obtain

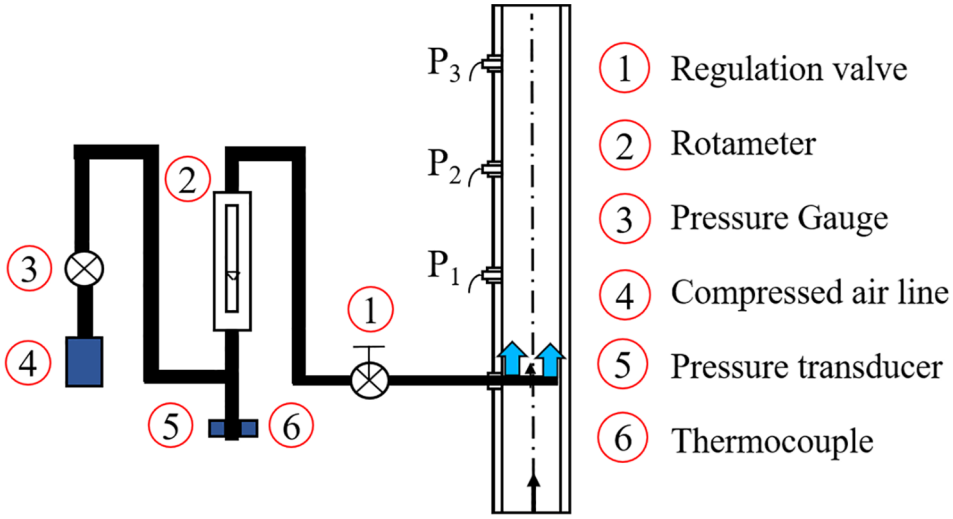

Fig. 11. Schematic set-up for the calibration of the 3PT technique: air is injected via a needle with three equidistantly spaced holes.

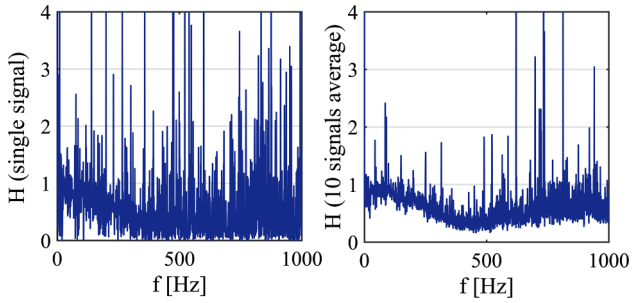

Fig. 12. Effect of averaging in time on H function (c = 106.30 m/s). Left: H function obtained for a single pressure measurement. Right: H function obtained by averaging 10 single pressure measurements.

cavitation. $\hat{P}$ is the dimensionless pressure drop (Eq. (13)) defined as the square root of the ratio between the pressure drop across the orifice and a term including the saturation pressure P_{sat} and the liquid critical pressure ratio F_f introduced by Stiles [41] and defined in Eq. (14). The term F_f takes into account the fact that the liquid vaporizes at a pressure lower than the saturation one because of thermodynamic non-equilibrium effects.

$$\hat{P} = \frac{\sqrt{P_{up} - P_{dw}}}{\sqrt{P_{up} - F_f \cdot P_{sat}}} \tag{13}$$

$$F_f = 0.96 - 0.28 \cdot \sqrt{\frac{P_{sat}}{P_{cri}}} \tag{14}$$

The cavitation intensity is not depending uniquely on the pressure drop but also on the pressure conditions upstream of the orifice. Hence, as explained by Pinho [42], the choice of $\hat{P}$ is useful to compare different working conditions among them. A first comparison can be observed by means of the hydraulic curve, flow rate Q versus pressure drop ΔP. We consider here a non-dimensional flow rate:

$$\hat{Q} = \frac{Q}{Q_{max}} \tag{15}$$

that is obtained by dividing Q by the maximum flow rate at a given upstream pressure which reads as:

$$Q_{max} = F_L \cdot K_v \cdot \sqrt{P_{up} - F_f \cdot P_{sat}} \tag{16}$$

where F_L is the liquid pressure recovery factor and K_v the orifice flow

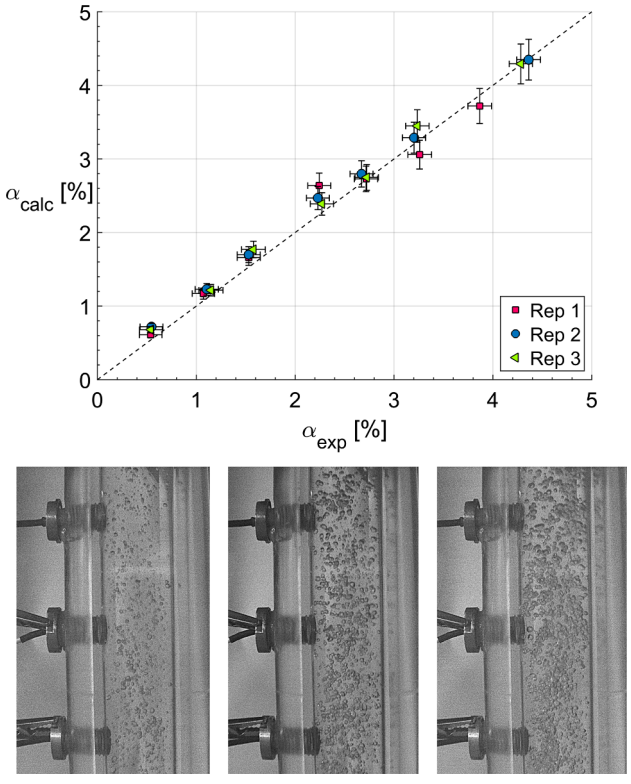

Fig. 13. Results of the validation study (top) and three examples of the instantaneous images captured at three different void fraction values, from left to right: a) 0.5%, b) 2.2%, c) 3.9% (bottom).

coefficient. Baumann [43] defines the F_L as the ratio between the overall pressure drop through an orifice and the drop between the static pressure at the inlet and the one at the *vena contracta*, Eq. (17). K_v is the volumetric flow rate of water which passes through a restriction with a pressure drop of 1 bar.The experimental K_v was computed for the two orifices and it is equal to 1.48 ± 0.04 $\frac{m^3/h}{\sqrt{bar}}$ for the cylindrical shape and equal to 1.07 ± 0.01 $\frac{m^3/h}{\sqrt{bar}}$ for the conical one.

$$F_L = \sqrt{\frac{P_{up} - P_{dw}}{P_{up} - P_{vc}}} \tag{17}$$

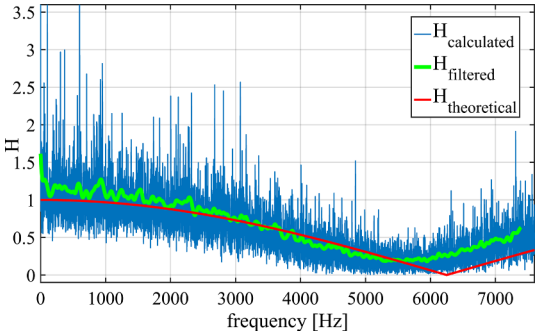

Fig. 14. Comparison between the filtered H function and the theoretical one.

Concerning the cavitation experimental campaign, the following procedure was followed. Before each test, the water is deaerated, first by slightly heating it at 30 °C while it circulates in the closed loop at the minimum pump speed, after by activating the vacuum pump to liberate the oxygen. The dissolved oxygen concentration is expressed as a percentage of the maximum amount of oxygen that water can hold at a given temperature, as in Eq. (18).

$$\%saturation = \left(\frac{actualDOreading\,[mg/L]}{saturatedDOreading\,[mg/L]} \right) \cdot 100 \tag{18}$$

While testing, different flow conditions are reached by fixing the downstream pressure and gradually increasing the upstream one. This procedure has been repeated for different downstream conditions ranging between 100 kPa and 10 kPa. For each testing condition data have been recorded for 10 s. Let's consider the cylindrical orifice. Five data sets (*T1*,*T2*,*T3*,*T4*,*T5*) were produced and they are summarized in Table 2. Different combinations of upstream and downstream velocity allowed flow conditions ranging from $\hat{P} = 0.23$ to $\hat{P} = 0.99$ which correspond to 0.11 kg/s$\leqslant Q \leq$ 0.70 kg/s ($5.36{\cdot}10^4 \leqslant Re \leqslant 1.76{\cdot}10^5$). Thus, an experimental matrix of 65 tests was analysed to explore all the possible cavitating conditions in our facility.

Fig. 15 illustrates the non-dimensional hydraulic curve obtained from the experimental data of these five data sets. Cavitation is triggered at $\hat{P}$ around 0.74. As shown in Fig. 16, the cavitation inception is witnessed by the sudden increase in the fluctuations measured by the pressure transducer placed 4.9D downstream of the orifice. Few tiny bubbles start to appear intermittently. However, the flow rate dependence on the square root of the pressure drop is still linear. Around $\hat{P} = 0.80$ cloud cavitation develops. Bubbles cluster into clouds which shed periodically downstream and eventually collapse. Further increases in $\hat{P}$ make cavitation to be stronger. The cavity size increases progressively up to stabilize the flow rate around a certain value corresponding to the choked flow condition. In the last part of the hydraulic curve, a further regime transformation is shown. This transition is called super-cavitation and it is documented by Yan and Thorpe [39]. A submerged liquid jet becomes visible at the centre of the test section, while a thick vapour cavity surrounds it and a film of water is falling down the walls of the test section.

6.2. 3PT technique in a cavitating flow

One of the hypotheses at the basis of the 3PT technique is that the flow should be considered homogeneous.

In our study, the aim is to characterize single orifices of different shapes which serve as a model to simulate the behaviour of valves in more complex piping systems. As it is shown in Fig. 17, in most of the regimes the flow immediately at the exit of the orifice is neither homogeneous nor steady and the interaction between the interface of the vapour clouds and the liquid is not clearly distinguishable. In addition, at increasing $\hat{P}$ the vapour clouds grow and occupy longer portions of the pipe downstream of the orifice exit.

Considering this issue, the position of the pressure sensors was chosen at a distance of 4.9 D downstream of the orifice (*FOV* 2). Fig. 18 illustrates that the flow in this region is mostly homogeneous. Either a fully liquid flow is visible because the pressure already recovered, or a bubbly flow appears since the vapour clouds at the orifice exit break before reaching *FOV* 2. It is important to underline that the 3PT technique is applied to the region where the downstream pressure used to draw the hydraulic curve of the orifice is also measured. By doing that, we think it is possible to get a link between the Mach number and the void fraction on one side, with the cavitation intensity and the orifice losses on the other.

Such a link could improve our understanding of the hydraulic behaviour of the tested orifices. In addition, a qualitative estimation of the cavitation damping along the pipe could be obtained by comparing the flow visualizations in *FOV* 1 and *FOV* 2.

Finally, the simultaneous presence of gas and vapour in cavitation bubbles is not taken into account in the theoretical formulation proposed by Brennen [44]. However, Shamsborhan [25] reported a good agreement between the experimental results and the theoretical relation for a two-phase two-species mixture. Furthermore, the analytical linear model for the propagation of pressure waves explained by Prosperetti [45] shows the reason why the presence of the vapour in addition to that of the gas does not affect the validity of such relation.

6.3. Application range of the 3PT technique

To assess the applicability of the 3PT technique to the different cavitating regimes, the global coherence function γ^2 was estimated. Firstly, the magnitude-squared coherence function $\gamma^2_{i,j}$ (Eq. (19)) was computed between two signals (i, j) acquired by two consecutive pressure transducers. So, $\gamma^2_{i,j}$ corresponds to the ratio between the cross-power spectral density (G_{ij}) and the power spectral densities of each pressure signal (G_{ii}, G_{jj}). The global coherence function is then defined as the half-sum of the squared coherence between P_1 and P_2 (*i. e.* $\gamma_{1,2}$) and that between P_3 and P_2 (*i. e.* $\gamma_{3,2}$), as reported in Eq. (20).

$$\gamma^2_{i,j} = \frac{|G_{i,j}(f)|^2}{G_{i,i}(f) \cdot G_{j,j}(f)} \tag{19}$$

$$\gamma^2 = \frac{1}{2} \cdot \left[\gamma^2_{1,2} + \gamma^2_{3,2} \right] \tag{20}$$

Fig. 19 depicts the obtained global coherence in four cases with increasing $\hat{P}$ and Re. By increasing the cavitation level, the frequencies range where the coherence is still reliable is drastically reduced. At $\hat{P} = 0.77$ (Fig. 19.a) the coherence is above 0.6 up to 7000 Hz. On the contrary, a coherence above 0.6 only concerns frequencies below 1500 if $\hat{P} = 0.92$ (Fig. 19.d). In this work, only the pressure measurements with $\gamma^2 \geqslant 0.6$ were considered valid. This threshold seemed reasonable both to have a good coherence between the signals and to ensure enough experimental points to evaluate the minimum of the H function for different testing conditions. Two examples of the resulting transfer functions are depicted in Fig. 20. When the cavitating flow reaches $\hat{P}$ as high as 0.98, the vapour cloud is denser and is visible in the measuring region (*FOV* 2). An example is shown in Fig. 21 with consequent degradation of the coherence function due to the poor homogeneity of the

Table 2
Test matrix for the cylindrical orifice.

	P_{dw} [kPa]	P_{up} [kPa] min÷max	Q [kg/s] min÷max
*T*1	100	200 ÷ 500	0.11 ÷ 0.67
*T*2	10	100 ÷ 300	0.20 ÷ 0.54
*T*3	20	100 ÷ 400	0.20 ÷ 0.67
*T*4	40	150 ÷ 300	0.40 ÷ 0.70
*T*5	50	200 ÷ 500	0.40 ÷ 0.70

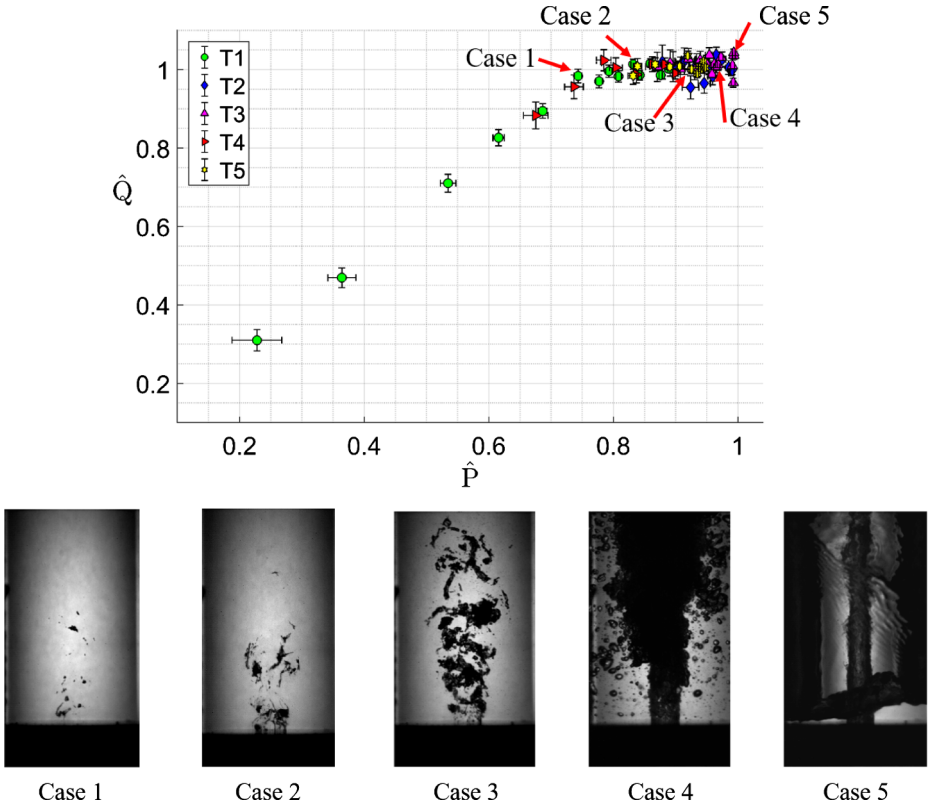

Fig. 15. Hydraulic curve for the cylindrical orifice with examples of the flow topology. Case 1: $\hat{P} = 0.78$; Case 2: $\hat{P} = 0.84$; Case 3: $\hat{P} = 0.92$; Case 4: $\hat{P} = 0.98$; Case 5: $\hat{P} = 1.00$.

flow.

6.4. Speed of sound measurements

The measurements performed with the cylindrical orifice geometry are first considered. In all the investigated test cases, the measured speeds of sound in *FOV* 2 ranged between 900 and 60 m/s. It is worth noticing that these values are relatively high for a two-phase water mixture, which is in line with the flow topology in *FOV* 2, as it was observed in Fig. 18. Considering these measures, as a first approximation, the velocity of the mixture in *FOV* 2 can be assumed equal to the velocity of the liquid upstream of the orifice. Therefore, a Mach number ($M_l = U_l/c$) was defined to represent the results from the whole set of data. Specifically, in Fig. 22 seven points are underlined and their corresponding instantaneous images are shown. The overall Mach number measured in the *FOV* 2 is very low, below 0.01. That is due to the flow re-stabilization at such a distance even if the cavitation is fully developed, $\hat{P} \geqslant 0.8$. As expected, the Mach number increases with the pressure drop, mainly due to a reduction in the speed of sound. For values of $\hat{P} < 0.9$ the flow is in single phase in *FOV* 2 and the Mach number corresponds to $M_l = 8.9{\cdot}10^{-4}$ (points A and B in Fig. 22). By increasing the pressure drop $\hat{P}$, a steep increase of the Mach number is observed. This is due to the fact that in this regime small changes in the pressure drop have a big impact on the cavitating flow topology which rapidly evolves towards the choked conditions. Fig. 22 highlights the markers corresponding to the conditions where a two-phase bubbly

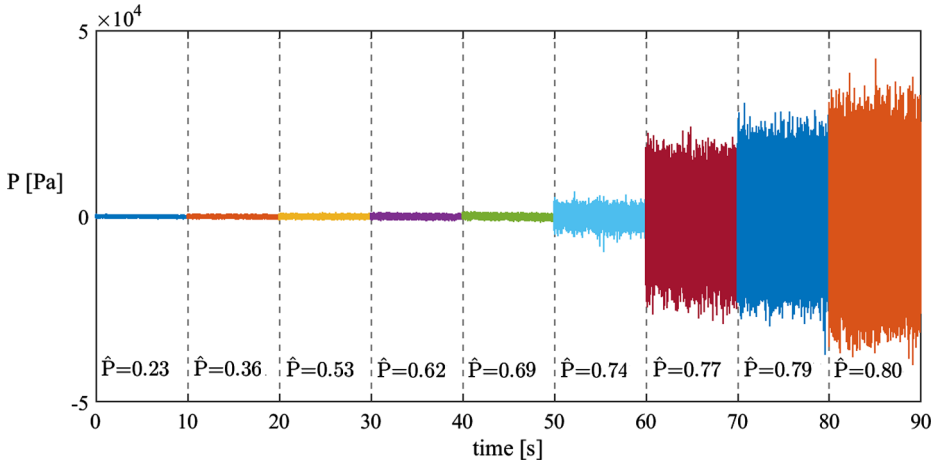

Fig. 16. Example of pressure fluctuations recorded 4.9D downstream of the orifice at increasing values of $\hat{P}$.

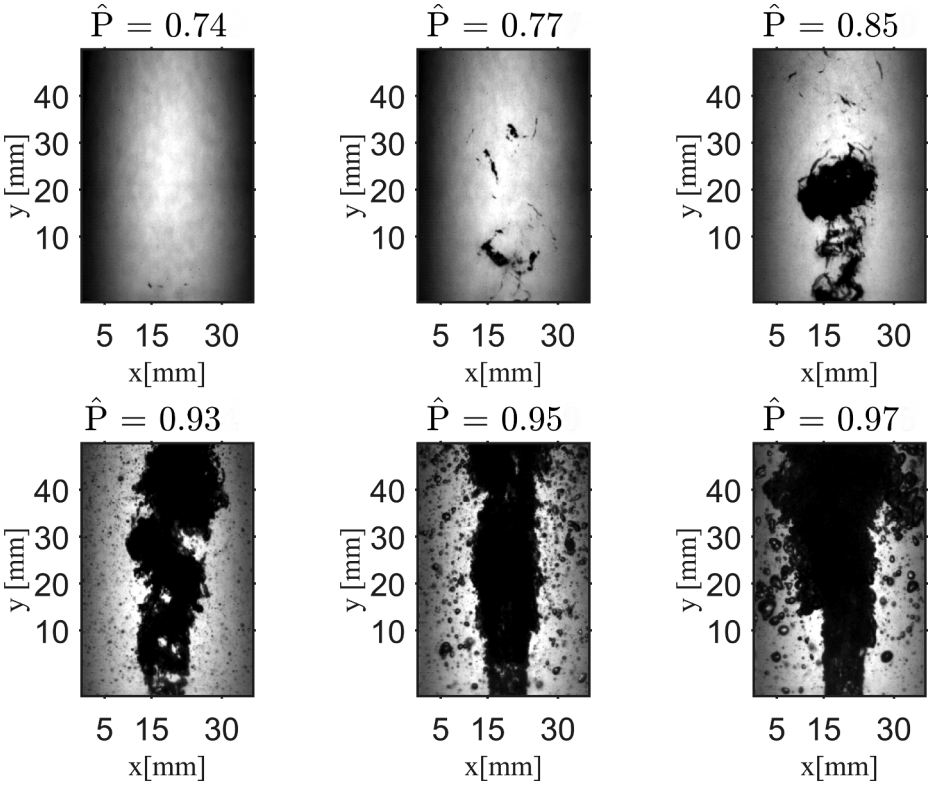

Fig. 17. Instantaneous images captured in *FOV* 1 at different $\hat{P}$: the vapor clouds shedding from the orifice form a continuous vapour jet for $\hat{P} \geqslant 0.90$.

flow is observed in *FOV* 2. All these points are well fitted by the exponential law which reads:

$$M_l = 2.\ 6{\cdot}10^{-4} e^{2.79||\hat{P}||} \tag{21}$$

Fig. 23 helps to visualize which is the range of applicability of the 3PT technique for the orifice under consideration. It is worth noticing that the first condition in which the speed of sound can be measured (Point A in Fig. 22) corresponds to the condition we identified as the

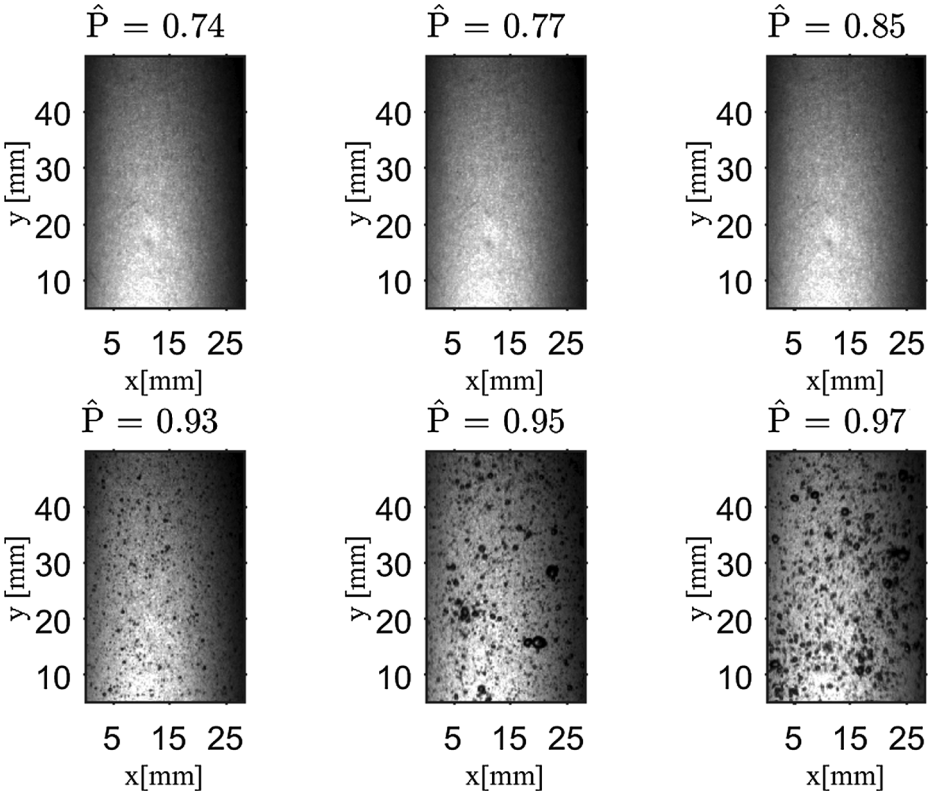

Fig. 18. Instantaneous images captured in *FOV* 2 at different $\hat{P}$: the vapor phase starts to be visible in FOV 2 for $\hat{P} \geqslant 0.90$.

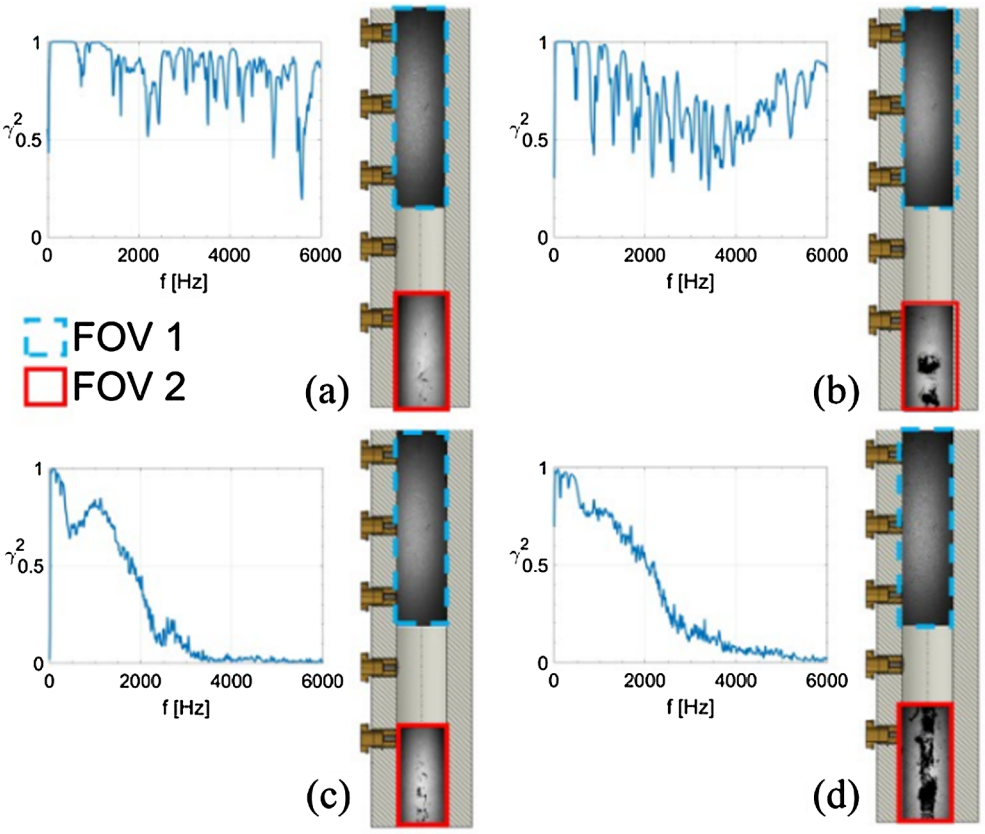

Fig. 19. Global coherence for: a) incipient cavitation with $Re = 1.69 \cdot 10^4$ and $\hat{P} = 0.77$; b) developed cavitation with $Re = 2.17 \cdot 10^4$ and $\hat{P} = 0.84$; c) incipient cavitation with $Re = 0.91 \cdot 10^4$ and $\hat{P} = 0.88$; d) developed cavitation with $Re = 1.05 \cdot 10^4$ and $\hat{P} = 0.92$.

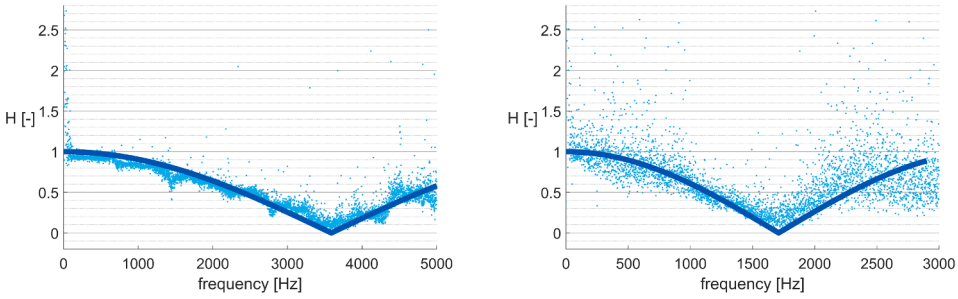

(a) H function for incipient cavitation at $Re = 1.69 \cdot 10^4$ and $\hat{P} = 0.77$

(b) H function for incipient cavitation at $Re = 0.91 \cdot 10^4$ and $\hat{P} = 0.88$

Fig. 20. Examples of the obtained *H* function.

cavitation inception for the cylindrical orifice ($\hat{P} = 0.74$). The rapid change in the Mach number for values of $\hat{P} \geqslant 0.9$ reflects the variety of cavitating flow topology which could be observed even once the orifice is already choked at the *vena contracta*. As pointed out in Section 6.3, the upper limit to the technique applicability is given by the extension of the main vapour cloud to the *FOV* 2.

Fig. 24 illustrates the results for the conical orifice. Again the measured speeds of sound fall in the same range measured for the cylindrical orifice. This is the range which gives a two-phase flow satisfying the 3PT technique hypothesis (i.e. homogeneity and plane wave hypothesis). Also for this orifice M_l exponentially grows with $\hat{P}$ once the bubbly two-phase flow reaches the *FOV* 2. A last attempt was performed by repeating the measurements with a third orifice, which was conical but with a $\beta = 0.30$. For such configuration with a larger β ratio, reliable measurements were only possible for few points at very low cavitation intensity ($c \approx 800$ m/s). This was due to the cavitating flow topology resulting from this orifice, i.e. the presence of big vapour structures which were easily evolving in super-cavitation regime.

6.5. Extension to the void fraction calculation

An estimation of the void fraction is provided by means of Eq. (6) which assumes the flow to be either adiabatic or isothermal. The suitability of this relation for a two-phase cavitating flow was shown by [25]. Therefore, the void fraction was computed with both models and the resulting difference was used to estimate the uncertainty in the computed value. However, using Eq. (6) alone could lead to the wrong value of α, since two solutions are possible for each speed of sound. That is why, the choice of the correct α is still guided by the flow visualizations within this study. The results are shown in Fig. 25 where

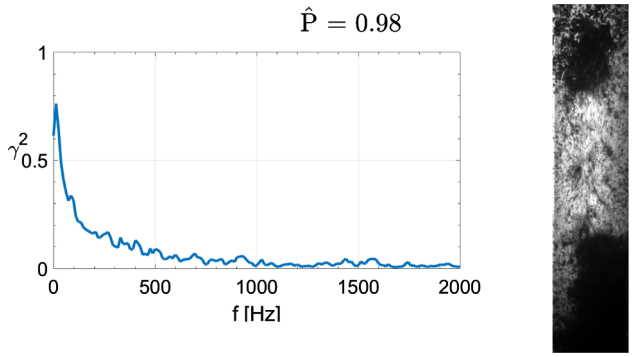

Fig. 21. Developed cavitation at $\hat{P} = 0.98$ and $Re = 9.45{\cdot}10^4$: the non-homogeneity of the flow causes the lost of coherence between the pressure measurements.

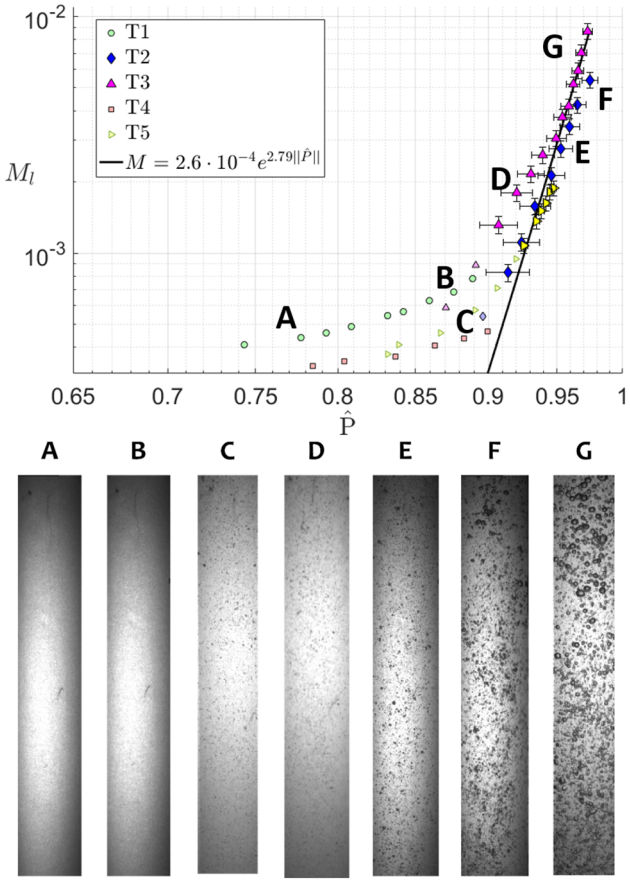

Fig. 22. Evolution of M_l with $\hat{P}$ becomes exponential when bubbles start appearing in *FOV* 2. Seven cases are highlighted with their corresponding instantaneous images (*FOV* 2).

the uncertainty increases with the value of α due to the larger variation between the adiabatic and isothermal model. At low void fractions, the discrepancy between the two curves is practically negligible. Not surprisingly, the overall level of the void fraction is extremely low, very far from the situation at the exit of the orifice. The results from different test cases have a certain degree of variance at the same $\hat{P}$. To clarify this behaviour, it is useful to observe the images from the flow in the *FOV* 2 region. The instantaneous images captured for the test cases *T3* and *T5* at $\hat{P} = 0.94$ are reported in Fig. 26 for both the fields of view (*FOV* 1 and *FOV* 2). The flow visualized on the left side of Fig. 26 (test case *T3*) has been performed with $P_{dw} = 16$ kPa. The images on the right side of Fig. 26 (test case *T5*) concern a $P_{dw} = 45$ kPa. Images from *FOV* 1

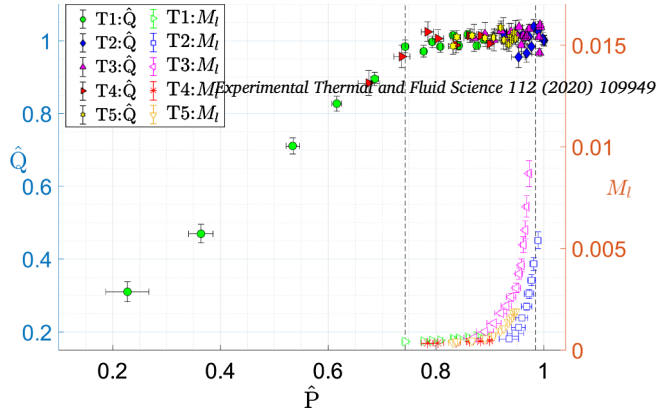

Experimental Thermal and Fluid Science 112 (2020) 109949

Fig. 23. Measured Mach number and non-dimensional flow rate as a function of $\hat{P}$ (cylindrical orifice).

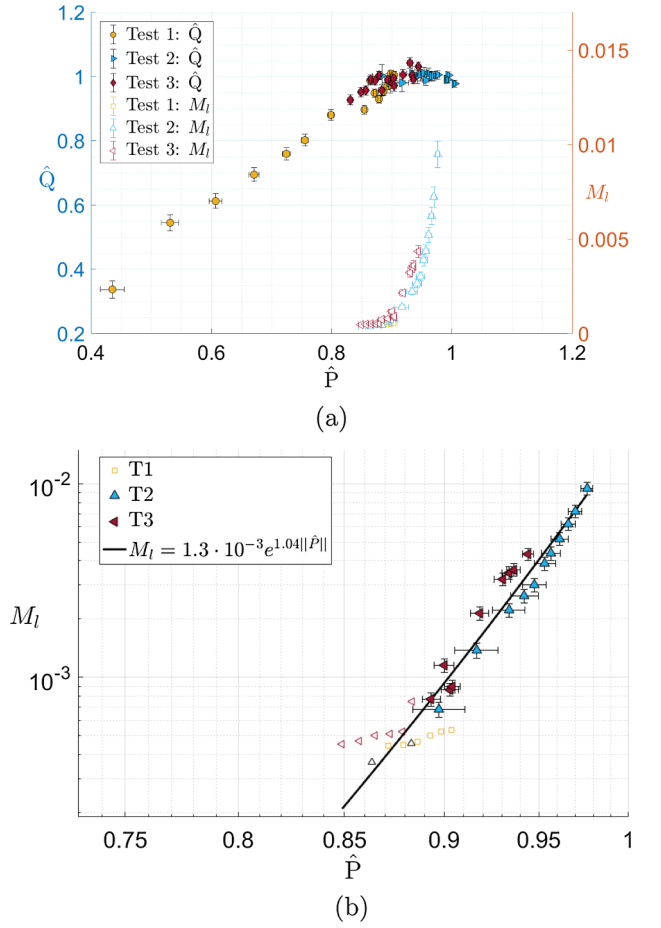

Fig. 24. Conical orifice: (a) Measured Mach number and non-dimensional flow rate as a function of $\hat{P}$; (b) Exponential evolution of M_l when bubbly flow reaches *FOV* 2.

(images c and d) show the same flow topology: a big vapour cloud is present at the exit of the orifice causing the choking of the flow. On the contrary, despite the same value of $\hat{P}$, two different conditions are obtained in terms of α because of the P_{dw}: $\alpha = 0.11\%$ for the test case with $P_{dw} = 16$ kPa and $\alpha = 0.03\%$ for the one with $P_{dw} = 45$ kPa. In fact, Fig. 26.a and Fig. 26.b show that a lower liquid pressure enhances the life and the growth of the bubbles increasing the void fraction level. This means that the downstream pressure is not adequately taken into account in the models used for the evaluation of the cavitation intensity.

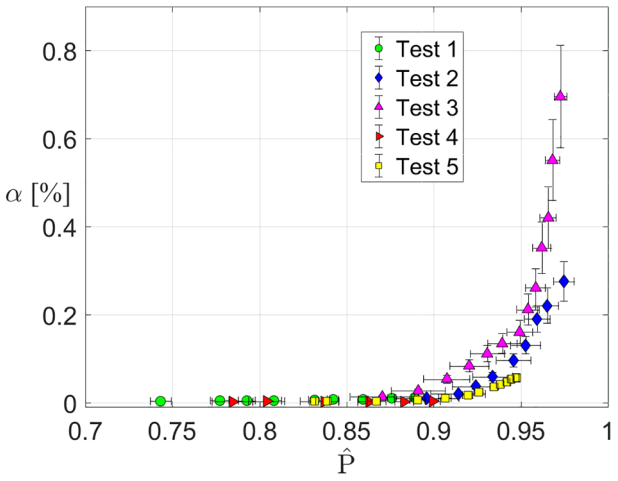

Fig. 25. Computed void fraction as a function of $\hat{P}$ for the cylindrical orifice.

7. Conclusions

In this work, we discussed the possibility to measure the speed of sound and the void fraction in a cavitating flow by means of the 3PT technique. Our interest in this technique is determined by its simple implementation, which could be helpful when the use of other techniques is hardened or in absence of visual access. The algorithm needed to implement the 3PT technique was developed to automatically compute the speed of sound in the test section from the measured pressure. Starting from artificial pressure signals, the effect of parameters such as the pressure transducers spacing and the sampling frequency on the accurate derivation of the speed of sound has been assessed. The presence of noise in the acquired signal was also considered to estimate the uncertainty in the results provided by this algorithm. It was found that the accuracy on the measurements mainly depends on the sampling frequency when high speeds of sound (ranging from 800 to 1500 m/s) are targeted. On the contrary, at low speeds of sound, the measurements are strongly affected by the level of noise.

The algorithm was then tested with a two-phase two-species mixture with a known level of void fraction and it gave speed of sound values in good agreement with the theoretical relation described in [44].

Finally, this algorithm was applied to the measurements in a real cavitating flow. The application of the 3PT in cavitating flow appeared to be not trivial. Firstly, the main limits of this technique were highlighted. Indeed, first tests revealed that the technique was not applicable in the regions close to the orifice where cavitation is triggered since both the homogeneous flow and the plane wave hypotheses are not fulfilled. As a consequence, the coherence between consecutive pressure signals was lost and the technique could not be applied. The algorithm gave accurate measurements when using the pressure signals acquired at a distance of 4.8 D from the orifice. Even if these measurements are not representative of the most critic conditions in a cavitating flow, they give information about the flow condition in the vicinity of the region where cavitation is induced and can be used as monitoring for flow quality control. For the studied test cases, c_{conf} was ranging from ~900 m/s (cavitation inception) to ~50 m/s (developed cavitation). M_l was observed to grow exponentially for values of $\hat{P} \geqslant 0.9$ where the two-phase flow also reaches the far-field, namely, *FOV* 2. This change in the evolution of the speed of sound occurs once the flow is already choked at the orifice and, at a macroscopic level, the behaviour of the orifice seems unaltered for further increases in $\hat{P}$. Nevertheless, this continuous reduction in the speed of sound seems to correspond to the actual evolution in the cavitating flow topology observed from the visualizations. This behaviour was observed for both the tested orifices suggesting a possible relation, at least qualitative,

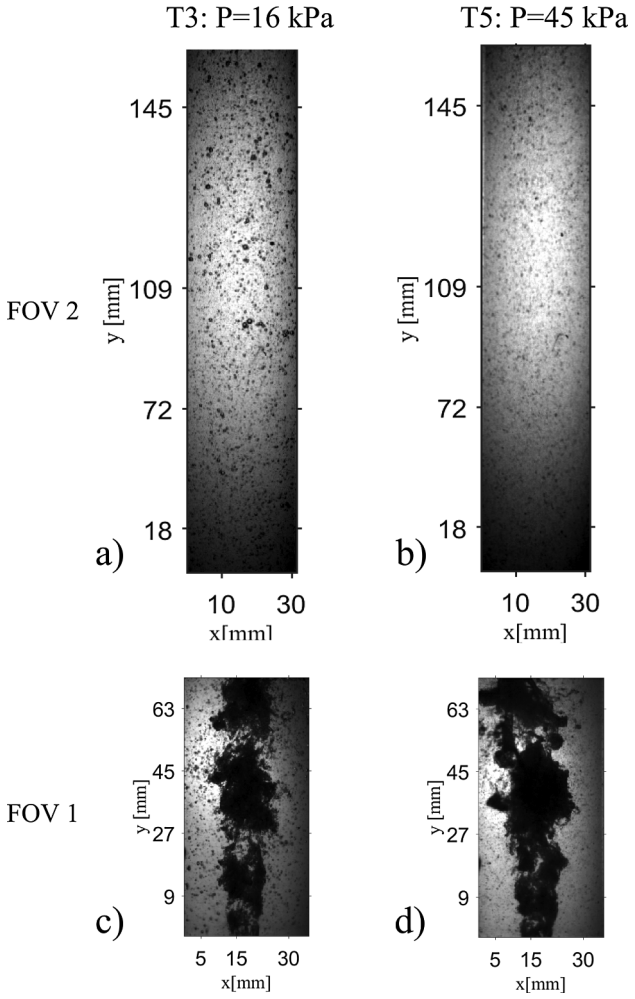

Fig. 26. Instantaneous images captured at $\hat{P} = 0.94$ but with different pressure downstream the orifice: $P = 16$ kPa for the test case 3 (a and c images); $P = 45$ kPa for the test case 5 (b and d images).

between what is occurring at the exit of the orifice and what we can measure downstream. Lastly, the validity of the theoretical formulation, Eq. (6), was assumed for cavitating flow to have a first estimation of the void fraction. Indeed, for this step, flow visualizations were crucial to discriminate between the two solutions provided by the equation. A comparison among the results from different test cases highlighted the role of the downstream liquid pressure in the measurements region, P_{dw}. Usually, the upstream pressure is the one identified as a key parameter controlling the cavitation regime and the evolution of the cavitation cloud shedding. However, the back pressure is the one which affects the life and the growth of the vapour bubbles, therefore, different back pressure led to different void fraction values.

To conclude, this paper aimed at exploring the limits and advantages offered from the 3PT technique when used in cavitating flows.

It would be valuable for future research to adopt a second technique to measure the void fraction both in the region where the three probes are located and at the orifice exit. These measurements, combined with the 3PTs, could help to validate the suitability of Brennen formulation and to extract a correlation that could describe the evolution of the cavitating flow along the pipe.

Declaration of Competing Interest

The authors declared that there is no conflict of interest.

Acknowledgements

This work is supported by the ESA's Networking/Partnering Initiative (NPI) grant 4000117725/16/*NL/MH/GM*. We gratefully acknowledge Dr. Jorge Pinho for the useful discussions.

References

[1] J. Jakobsen, On the mechanism of head breakdown in cavitating inducers, J. Basic Eng. 86 (2) (1964) 291–305.
[2] A. Danlos, F. Ravelet, O. Coutier-Delgosha, F. Bakir, Cavitation regime detection through proper orthogonal decomposition: dynamics analysis of the sheet cavity on a grooved convergent–divergent nozzle, Int. J. Heat Fluid Flow 47 (2014) 9–20.
[3] H. Ganesh, S.A. Mäkiharju, S.L. Ceccio, Bubbly shock propagation as a mechanism for sheet-to-cloud transition of partial cavities, J. Fluid Mech. 802 (2016) 37–78.
[4] M. Callenaere, J.-P. Franc, J.-M. Michel, M. Riondet, The cavitation instability induced by the development of a re-entrant jet, J. Fluid Mech. 444 (2001) 223–256.
[5] S. Jahangir, E.G. Wagner, R.F. Mudden, C. Poelma, X-ray computed tomography of cavitating flow in a converging-diverging nozzle, in: CAV2018, 2018.
[6] E. Goncalves, R.F. Patella, Numerical simulation of cavitating flows with homogeneous models, Comput. Fluids 38 (9) (2009) 1682–1696.
[7] J. Decaix, E. Goncalves, Time-dependent simulation of cavitating flow with k-turbulence models, Int. J. Numer. Meth. Fluids 68 (8) (2012) 1053–1072.
[8] F. Örley, T. Trummler, S. Hickel, M. Mihatsch, S. Schmidt, N. Adams, Large-eddy simulation of cavitating nozzle flow and primary jet break-up, Phys. Fluids 27 (8) (2015) 086101.
[9] O. Coutier-Delgosha, J. Reboud, Y. Delannoy, Numerical simulation of the unsteady behaviour of cavitating flows, Int. J. Num. Methods Fluids 42 (5) (2003) 527–548.
[10] D. Leppinen, S. Dalziel, A light attenuation technique for void fraction measurement of microbubbles, Exp. Fluids 30 (2) (2001) 214–220.
[11] S.L. Ceccio, C.E. Brennen, Observations of the dynamics and acoustics of travelling bubble cavitation, J. Fluid Mech. 233 (1991) 633–660.
[12] D.L. George, C.O. Iyer, S.L. Ceccio, Measurement of the bubbly flow beneath partial attached cavities using electrical impedance probes, J. Fluids Eng. 122 (1) (2000) 151–155.
[13] Q. Wu, M. Ishii, Sensitivity study on double-sensor conductivity probe for the measurement of interfacial area concentration in bubbly flow, Int. J. Multiph. Flow 25 (1) (1999) 155–173.
[14] B.R. Elbing, S. Mäkiharju, A. Wiggins, M. Perlin, D.R. Dowling, S.L. Ceccio, On the scaling of air layer drag reduction, J. Fluid Mech. 717 (2013) 484–513.
[15] G. Lucas, R. Mishra, Measurement of bubble velocity components in a swirling gas–liquid pipe flow using a local four-sensor conductance probe, Meas. Sci. Technol. 16 (3) (2005) 749.
[16] O. Coutier-Delgosha, J.-F. Devillers, T. Pichon, A. Vabre, R. Woo, S. Legoupil, Internal structure and dynamics of sheet cavitation, Phys. Fluids 18 (1) (2006) 017103.
[17] B. Stutz, J.-L. Reboud, Measurements within unsteady cavitation, Exp. Fluids 29 (6) (2000) 545–552.
[18] T.J. Heindel, A review of X-ray flow visualization with applications to multiphase flows, J. Fluids Eng. 133 (7) (2011) 074001.
[19] D. Bauer, H. Chaves, C. Arcoumanis, Measurements of void fraction distribution in cavitating pipe flow using X-ray ct, Measur. Sci. Technol. 23 (5) (2012) 055302.
[20] H. Hassis, Noise caused by cavitating butterfly and monovar valves, J. Sound Vib. 225 (3) (1999) 515–526.
[21] R. Henry, M. Grolmes, H.K. Fauske, Pressure-pulse propagation in two-phase one- and two-component mixtures., Tech. Rep., Argonne National Lab., Ill, 1971.
[22] D.L. Gysling, M.R. Myers, Distributed sound speed measurements for multiphase flow measurement, uS Patent 6,813,962, Nov. 9 2004.
[23] D. Margolis, F. Brown, Measurement of the propagation of long-wavelength disturbances through turbulent flow in tubes, J. Fluids Eng. 98 (1) (1976) 70–78.
[24] P. Testud, P. Moussou, A. Hirschberg, Y. Aurégan, Noise generated by cavitating single-hole and multi-hole orifices in a water pipe, J. Fluids Struct. 23 (2) (2007) 163–189.
[25] H. Shamsborhan, Développement d'une méthode de mesure de la célérité du son en écoulement diphasique application aux écoulements cavitants, Ph.D. thesis, Arts et Métiers ParisTech, 2009.
[26] A. Kashima, P.J. Lee, R. Nokes, Numerical errors in discharge measurements using the kdp method, J. Hydraulic Res. 50 (1) (2012) 98–104.
[27] G. Blommaert, Étude du comportement dynamique des turbines francis: contrôle actif de leur stabilité de fonctionnement, Ph.D. thesis, Verlag nicht ermittelbar, 2000.
[28] A. Simon, J.-J. Martinez-Molina, R. Fortes-Patella, A new process to estimate the speed of sound using three-sensor method, Exp. Fluids 57 (1) (2016) 10.
[29] C.E. Brennen, C.E. Brennen, Fundamentals of Multiphase Flow, Cambridge University Press, 2005.
[30] J. Lighthill, Waves in Fluids, Cambridge University Press, 1978.
[31] G. Costigan, P. Whalley, Measurements of the speed of sound in air-water flows, Chem. Eng. J. 66 (2) (1997) 131–135.
[32] L. Carlucci, J. Brown, Experimental studies of damping and hydrodynamic mass of a cylinder in confined two-phase flow, J. Vib. Acoust. Stress Reliab. Des. 105 (1) (1983) 83–89.
[33] C. Charreton, C. Béguin, A. Ross, S. Etienne, M. Pettigrew, Two-phase damping in vertical pipe flows: Effect of void fraction, flow rate and external excitation, ASME 2014 Pressure Vessels and Piping Conference, American Society of Mechanical Engineers, 2014pp. V004T04A048–V004T04A048.
[34] G. Hewitt, D. Roberts, Studies of two-phase flow patterns by simultaneous X-ray and flast photography, 1969.
[35] Y. Taitel, D. Bornea, A.E. Dukler, Modelling flow pattern transitions for steady upward gas-liquid flow in vertical tubes, AIChE J. 26 (3) (1980) 345–354, https://doi.org/10.1002/aic.690260304.
[36] D. Chisholm, Void fraction during two-phase flow, J. Mech. Eng. Sci. 15 (3) (1973) 235–236, https://doi.org/10.1243/jmes_jour_1973_015_040_02.
[37] S.L. Smith, Void fractions in two-phase flow: A correlation based upon an equal velocity head model, Proc. Inst. Mech. Eng. 184 (1) (1969) 647–664, https://doi.org/10.1243/pime_proc_1969_184_051_02.
[38] J.P. Tullis, Cavitation guide for control valves, Tech. Rep., Nuclear Regulatory Commission, Washington, DC (United States). Div. of Engineering; Tullis Engineering Consultants, Logan, UT (United States), 1993.
[39] Y. Yan, R. Thorpe, Flow regime transitions due to cavitation in the flow through an orifice, Int. J. Multiphase Flow 16 (6) (1990) 1023–1045.
[40] C. Mishra, Y. Peles, Cavitation in flow through a micro-orifice inside a silicon microchannel, Phys. Fluids 17 (1) (2005) 013601.
[41] G. Stiles, Cavitation and flashing considerations, ISA Handbook of Control Valves, 2nd Edition by Hutchinson, JW (1976) 206–211.
[42] J. Pinho, J.-M. Buchlin, S. Chabane, B. Haut, Experimental investigation of cavitation in a safety relief valve using water: extension to cryogenic fluids, 2015.
[43] H.D. Baumann, The introduction of a critical flow factor for valve sizing, ISA Trans. 2 (2) (1963).
[44] C.E. Brennen, Cavitation and Bubble Dynamics, Cambridge University Press, 2013.
[45] A. Prosperetti, The speed of sound in a gas–vapour bubbly liquid, Interface Focus 5 (5) (2015) 20150024.